Rare Met. (2023) 42(3):806–812
https://doi.org/10.1007/s12598-022-02212-w

RARE METALS

LETTER

Hydropathy modulation on Bi_2S_3 for enhanced electrocatalytic CO_2 reduction

Long-Sheng Zhan, Yu-Chao Wang, Meng-Jie Liu, Xin Zhao, Jiao Wu, Xiang Xiong, Yong-Peng Lei*

Received: 15 September 2022 / Revised: 26 September 2022 / Accepted: 27 September 2022 / Published online: 1 December 2022

Electrochemical CO_2 reduction reaction (CO_2RR) is a promising way to achieve carbon neutrality. However, the activity and selectivity of CO_2RR are limited by not only the development of earth-abundant catalysts but also the CO_2 mass transfer during the CO_2RR process. Herein, Bi_2S_3 nanorods were synthesized under a relatively mild route. Furthermore, benefitting to the modulation of the hydropathy, the optimized sample (BS-P1) achieved a Faradaic efficiency of $HCOO^-$ (> 90%) in the range from − 0.9 to − 1.2 V, a high current density of $HCOO^-$ (2.29 times larger than that of BS-P0 at − 1.2 V) and a prolonged stability from 12 to 20 h at − 1.1 V. When the temperature decreased from 25 to 0 °C and eventually to − 20 °C, the reaction kinetics of CO_2RR was slowed down, the distribution of products was changed and hydrogen evolution reaction (HER) was inhibited. This work provides a facile synthesis for Bi_2S_3 and highlights the importance of triple-phase interfaces in CO_2RR.

To solve the issue of excessive emission of CO_2, many strategies have been proposed [1–5]. Electrochemical CO_2 reduction reaction (CO_2RR), driven by renewable electricity, could convert CO_2 into value-added industrial feedstock [6–11]. However, the low selectivity, small current density, poor stability, etc., must be overcome [12–15]. As one of products in CO_2RR, formate/formic acid ($HCOO^-$/HCOOH) was important chemical intermediates in industrial process [16–18]. Many efforts had been devoted to improving selectivity of products. However, enhancement of current density was more urgent. Only with high current density of $HCOO^-$/HCOOH production will CO_2RR possess the potential for industrial application [1, 2, 8]. Compared with other metallic materials (e.g., Pd, In, Sn), Bi-based materials were one of the potential candidates for formic acid due to their low toxicity, earth-abundance and good selectivity [19–24]. Generally, Bi_2S_3 is prepared under complex conditions (e.g., multi-steps, usage of strong acids, high reaction temperature, long reaction time, etc.) (Table S1). Zhang et al. [25] reported the synthesis of urchin-like Bi_2S_3 using the solvothermal method holding at 240 °C for 24 h, the maximum Faradaic efficiency of $HCOO^-$ (FE_{HCOO-}) was 84.0% at − 0.75 V versus reversible hydrogen electrode (RHE), but it suffered from low current density of $HCOO^-$ (J_{HCOO-}) ≈ − 6 mA·cm^{-2}. On the other hand, tripe-phase interfaces regulation could enhance mass transport and local concentration of reaction species [26–29]. Sun et al. studied the hydrophobicity of the interface of Cu nanoarray electrode for CO_2RR, which could change the distribution of products [30].

Herein, we synthesized Bi_2S_3 nanorods under relatively mild conditions and tuned their hydropathy by adding polytetrafluoroethylene (PTFE) nanoparticles into catalyst ink. The optimized sample (BS-P1) achieved a FE_{HCOO-} of 93.4% at − 1.1 V, and the J_{HCOO-} was 2.29 times larger than that of BS-P0 (without modification) at − 1.2 V.

Supplementary Information The online version contains supplementary material available at https://doi.org/10.1007/s12598-022-02212-w.

L.-S. Zhan, Y.-C. Wang, M.-J. Liu, X. Zhao, X. Xiong, Y.-P. Lei*
State Key Laboratory of Powder Metallurgy, Powder Metallurgy Research Institute, Central South University, Changsha 410083, China
e-mail: lypkd@163.com; leiyongpeng@csu.edu.cn

J. Wu
School of Material Science and Engineering, Central South University of Forestry and Technology, Changsha 410004, China

Also, the stability of Bi_2S_3 was extended from 12 to 20 h by tuning hydropathy. In flow cells, $FE_{HCOO^-} > 90\%$ at from − 0.5 to − 0.75 V with increased current density. Hydrophobicity of interfaces could accelerate CO_2 mass transfer, thus enhancing CO_2RR performance. The influence of temperature for CO_2RR was also investigated.

Universally, the synthesis conditions of Bi_2S_3 were generally complex (e.g., strong acids and high temperatures, etc.) (Table S1). Then we prepared Bi_2S_3 under mild conditions. The Bi_2S_3 nanorods were synthesized from $BiCl_3$ and TAA in ethanol at 150 °C (Figs. 1a and S1). First, we explored the ratio of $BiCl_3$ to TAA, called as BS-5/2, BS-3/1, BS-10/3 (BS-P0) and BS-11/3, respectively. X-ray diffraction (XRD) was used to investigate the crystal structure for the catalysts. The main peaks of BS located at 24.9° and 28.6° were consistent with (130) and (211) planes in standard card of Bi_2S_3 (PDF No. 17-0320), respectively (Fig. 1b). Then PTFE nanoparticles were added in catalyst ink (see the detail in SI). According to the amounts of PTFE added, the catalysts were called as BS-Px (x = 0, 0.5, 1, 2). Peak at 18.1° was a characteristic peak of PTFE (PDF No. 47-2217) [31]. As the amount of added PTFE increased, characteristic peak of F was enhanced. Then the Bi 4f spectra of BS-P0 and BS-P1 are shown in Fig. 1c, and two peaks at 158.2 and 163.6 eV corresponded to Bi $4f_{7/2}$ and Bi $4f_{5/2}$, respectively. Also, peaks at 160.9 and 162.0 eV were related to Bi–S vibration [32]. Peaks at 158.6 and 164.3 eV would correspond to Bi–O vibration, which was mainly due to oxidation in air [33]. After adding PTFE, the peaks of FTFE were be detected, but the peaks intensity of Bi 4f spectrum become weaker (Fig. S2). X-ray photoelectron spectroscopy (XPS) is a surface detection

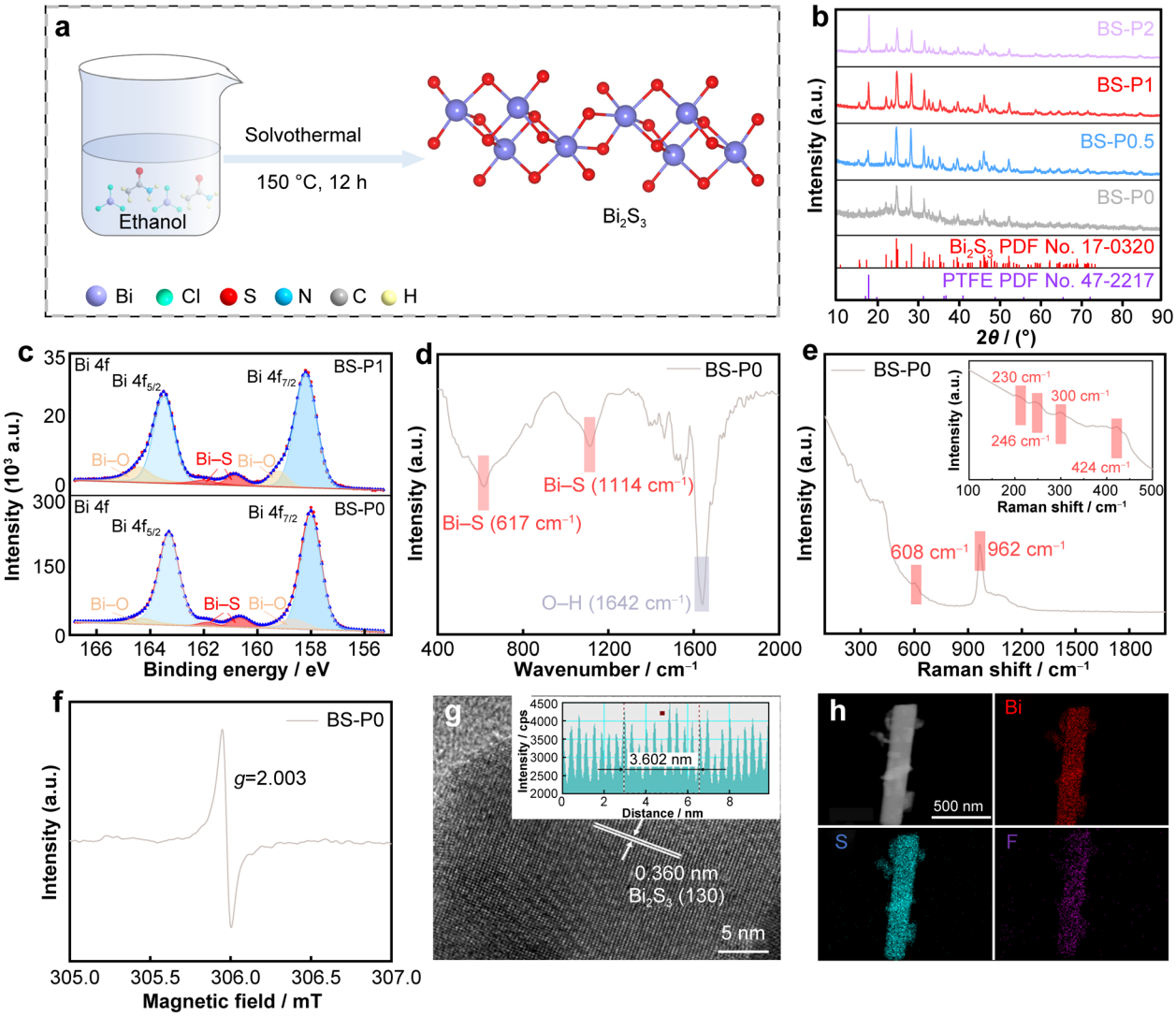

Fig. 1 **a** Schematic illustration for synthesis of Bi_2S_3; **b** XRD patterns; **c** Bi 4f XPS result; **d** FTIR of BS-P0; **e** Raman spectrum of BS-P0 (inset: Raman spectrum in range of 100–500 cm^{-1}); **f** EPR of BS-P0; **g** HRTEM image of BS-P0 (inset: line intensity profile); **h** EDS elemental mappings images of BS-P1

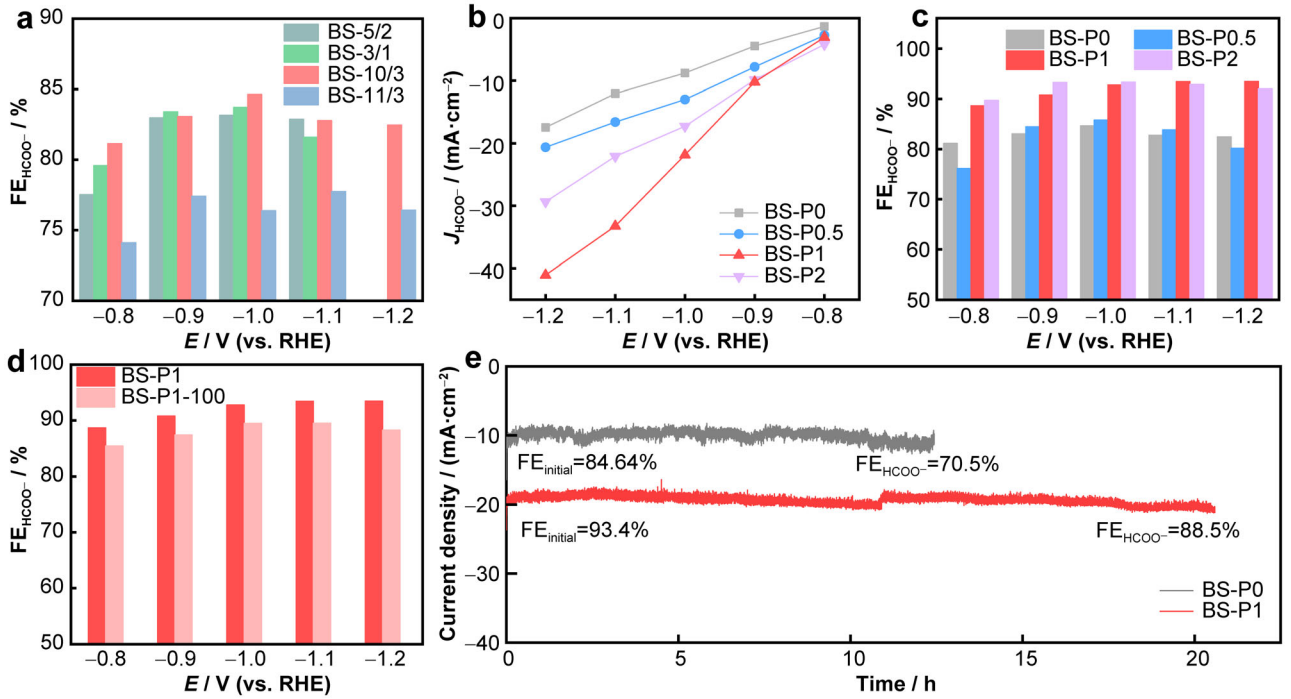

Fig. 2 **a** FE$_{HCOO^-}$ of BS with different amounts of TAA; **b** J_{HCOO^-} and **c** FE$_{HCOO^-}$ of different samples; **d** comparison of FE$_{HCOO^-}$ with different PTFE particle sizes; **e** stability at − 1.0 V of BS-P1 and BS-P0 in H-type cells

technique. The addition of PTFE reduced the amount of Bi_2S_3 detectable on the electrode surface. XPS results showed that PTFE was successfully loaded on the surface of Bi_2S_3 nanorods.

In the Fourier transform infrared (FTIR) spectra presented in Fig. 1d, the bands at 617 and 1114 cm^{-1} could be assigned to Bi–S vibration. The band at 1642 cm^{-1} was assigned to O–H stretching vibrations due to the adsorption of water on surface of BS-P0 [34]. The Raman spectrum of BS-P0 is provided in Fig. 1e, and Raman bands located at 230, 246, 300, 424, 608 and 962 cm^{-1} could be observed, matching with the Raman feature of Bi_2S_3 [35–37]. No carbon species were found in BS-P0. The isotropic electron paramagnetic resonance (EPR) signals at $g = 2.003$ in Fig. 1f were observed. They could be ascribed to the formation of sulfur vacancies, which may be good for CO_2RR [7].

The crystal structure was revealed by high-resolution transmission electron microscope (HRTEM) [38]. In Fig. 1g, the crystalline phase with interatomic distance of 0.360 nm can be related to Bi_2S_3 (130) plane. The result of HRTEM was consistent with that of XRD patterns. Energy-dispersive X-ray spectroscopy (EDS) elemental mappings revealed that the width of the Bi_2S_3 nanorod was ~ 200 nm. The morphology of Bi_2S_3 did not change with the addition of PTFE. Also, EDS elemental mappings confirm a relatively uniform distribution of PTFE (Figs. 1h and S3).

The electrochemical performance of CO_2RR was then investigated in H-type cells with 0.5 mol·L^{-1} $KHCO_3$ [39]. The final products (included gas products and liquid products) were measured by gas chromatography and nuclear magnetic resonance (NMR) spectroscopy (Fig. S4) [40]. Considering that the optimal ratio of TAA and $BiCl_3$ was 10/3 (Fig. 2a), the BS-P0 (10/3) was selected as the optimized sample. The current density in CO_2 was larger than that in Ar, indicating the electrocatalytic activity toward CO_2RR (Fig. S5) [41]. To compare their selectivity in CO_2RR, the constant voltage electrolysis methods were used (Fig. S6). The final products were only $HCOO^-$, CO and H_2. Sum of FE was close to 100%, and no other products were detected. With adding PTFE nanoparticles (200 nm), J_{HCOO^-} increased. Excessive PTFE led to the reduction of J_{HCOO^-}. The maximum J_{HCOO^-} of BS-P1 could reach − 41.08 mA·cm^{-2} at − 1.2 V, but J_{HCOO^-} of BS-P0 only was − 17.45 mA·cm^{-2} (Fig. 2b). BS-P1 has the largest J_{HCOO^-} in the range from − 0.9 to − 1.2 V with FE$_{HCOO^-}$ above 90%. Then FE$_{HCOO^-}$ of BS-P1 could reach 93.4% at − 1.1 V. In comparison, for BS-P0, the maximum FE$_{HCOO^-}$ was 84.64% at − 1.0 V (Fig. 2c). When the size of PTFE nanoparticles changed from 200 to 100 nm,

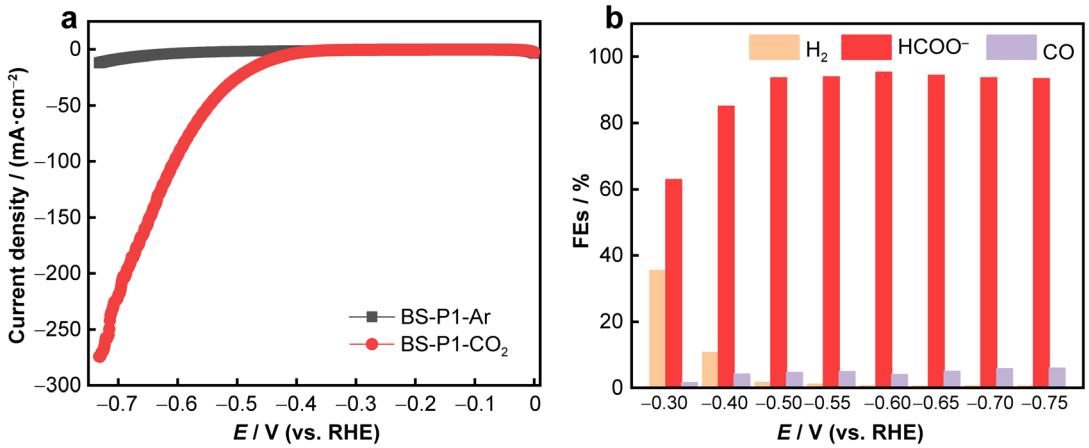

Fig. 3 **a** LSV curves of BS-P1 under different atmospheres and **b** FEs under different voltages of BS-P1 in standard three-electrode flow cells

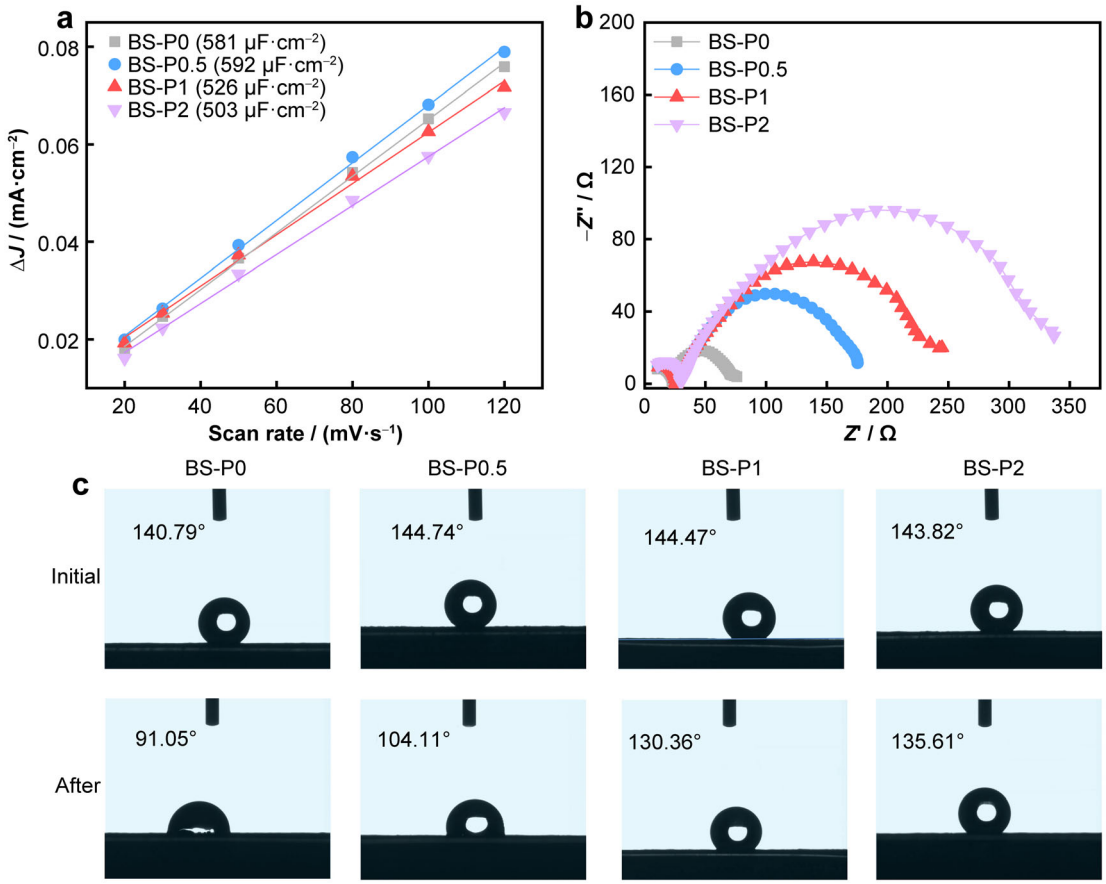

Fig. 4 **a** ECSA measurement; **b** EIS results; **c** contact angle measurements on BS electrode with different PTFE loadings before and after CO_2 electrolysis at − 1.0 V in H-type cells

FE_{HCOO^-} reduced (Figs. 2d and S7). Then FE_{HCOO^-} of BS-P1 still remained 88.5% at − 1.0 V after 20 h, while the FE_{HCOO^-} of BS-P0 was only 70.5% at − 1.0 V after 12 h (Fig. 2e). BS-P1 had a relatively good CO_2RR performance in the H-type cells (Fig. S8 and Table S2) [42].

Then we assembled the standard three-electrode flow cells with 1.0 mol·L^{-1} KOH as electrolyte [43]. A higher current density (200 mA·cm^{-2} at − 0.69 V) was obtained than that in H-type cells (Fig. 3a). FE_{HCOO^-} was larger than 93% in the potential range from − 0.50 to − 0.75 V. The

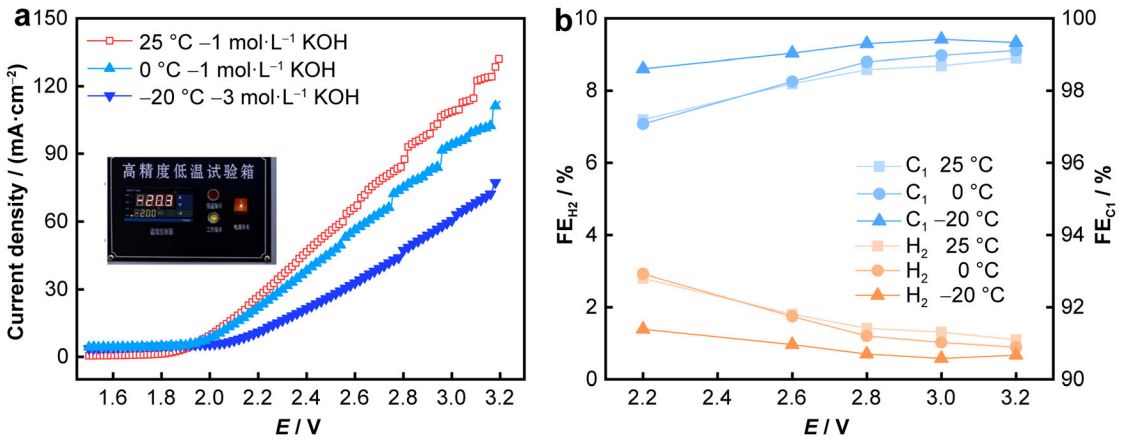

Fig. 5 **a** LSV curves (inset: optical photograph of low-temperature control device) and **b** FE of BS-P1 at different temperatures in two-electrode flow cells

maximum FE_{HCOO^-} reached 95.38% at − 0.6 V (Figs. 3b and S9).

As shown in Figs. 4a and S10, adding 0.5% PTFE nanoparticles had a little effect on the electrochemical active surface areas (ECSA), which was evaluated by the electric double-layer capacitance (C_{dl}) method [44]. Compared to BS-P0 (581 μF·cm^{-2}), ECSAs of BS-P1 and BS-P2 were significantly reduced to 526 and 503 μF·cm^{-2}, respectively, because of hydropathy modulation of triple-phase interfaces by adding PTFE, which could retain gas and reduce contact between electrolyte and electrode surface [45]. On the other hand, the ECSA of BS-P2 reduced nearly 13.4% of BS-P0. It meant that less electrolyte contacted with the electrode surface, which was the reason of the reduced CO_2 activity compared with BS-P1 (Fig. S5).

To investigate the intrinsic impedance of the catalyst, we tested the electrochemical impedance spectroscopy (EIS) without CO_2. EIS results showed that adding PTFE increased charge transfer resistance due to the poor conductivity of PTFE [46]. However, PTFE could change the microenvironment of the triple-phase interfaces on the electrode, thus influencing the J_{HCOO^-} (Figs. 4b, 2b). A lower Tafel slope of 159.82 mV·dec^{-1} on BS-P1 than that on BS-P0 (209.69 mV·dec^{-1}) suggested the accelerated reaction kinetics (Fig. S11) [47].

In Fig. 4c, the initial contact angles of BS-P0 (140.79°), BS-P0.5 (144.74°), BS-P1 (144.47°) and BS-P2 (143.82°) were similar. When BS with different PTFE amounts were electrolyzed at − 1.0 V for 1 h, the contact angle of BS-P0 decreased from 140.79° to 91.05° and the contact angle with 1% PTFE decreased from 144.47° to 130.36°. And with the increase in PTFE amounts, the contact angle after electrolysis also showed an increasing trend, which was larger than that of BS-P0. It meant that moderate hydrophobicity of triple-phase interfaces increased the CO_2RR performance. The hydrophobicity of interfaces accelerated CO_2 mass transfer and reduced the availability of electrolyte [48]. When 2% PTFE was added, the current density was dropped because of the lost balance between gas and liquid phases (Fig. S5).

Considering future extraterrestrial planet exploration, such as Mars, the performance of CO_2RR at low temperature is worth studying. However, the research of CO_2RR at low temperature was rare [49]. Here, as temperature decreased (25 to − 20 °C), the current density decreased (Fig. 5a). Compared with BS-P1 at 25 °C, the onset potential of BS-P1 at − 20 °C shifted to a more positive value, implying a slower CO_2RR kinetics [50]. In Fig. 5b, the peak FE_{C1} of BS-P1 reached 99.42% at 2.8 V, while the competing hydrogen evolution reaction (HER) on BS-P1 was substantially suppressed. The inhibition of HER may be due to the inhibition of the Volmer reaction of HER under alkaline conditions [51]. FE_{CO} of BS-P1 was increased with temperature decreasing (Figs. S12, S13).

In summary, Bi_2S_3 nanorods were synthesized under a mild condition. Then we added PTFE nanoparticles with different sizes (200 and 100 nm) into the catalyst ink to regulate the hydropathy of electrode surface. The J_{HCOO^-} and stability of Bi_2S_3 were improved more than two folds. Also, a high FE_{HCOO^-} was achieved (93.4% at − 1.2 V). Thus, this work not only provides a relatively mild route to synthesize Bi_2S_3, but also further improves the current density and stability of Bi_2S_3 through hydropathy modulation. By adding PTFE nanoparticles, the transition from hydrophobic to hydrophilic of electrode surface could be effectively slowed down during CO_2RR, which was the reason of enhanced CO_2RR performance. In addition, the

influence of temperature in the CO_2RR was studied, which could change the distribution of products. However, research on low-temperature CO_2RR is rare. The mechanism of inhibition of HER at low temperature is explored underway.

Acknowledgements This work was financially supported by the Fundamental Research Funds for the Central Universities of Central South University (No. 2022ZZTS0579).

Declarations

Conflict of interests The authors declare that they have no conflict of interest.

References

[1] Jiang ZL, Wang T, Pei JJ, Shang HS, Zhou DN, Li HJ, Dong JC, Wang Y, Cao R, Zhuang ZB, Chen WX, Wang DS, Zhang JT, Li YD. Discovery of main group single Sb-N_4 active sites for CO_2 electroreduction to formate with high efficiency. Energy Environ Sci. 2020;13:2856. https://doi.org/10.1039/D0EE01486A.

[2] Zhang JW, Sewell CD, Huang HW, Lin ZQ. Closing the anthropogenic chemical carbon cycle toward a sustainable future via CO_2 valorization. Adv Energy Mater. 2021;11(47):2102767. https://doi.org/10.1002/aenm.202102767.

[3] Wang YC, Liu Y, Liu W, Wu J, Li Q, Feng QG, Chen ZY, Xiong X, Wang DS, Lei YP. Regulating the coordination structure of metal single atoms for efficient electrocatalytic CO_2 reduction. Energy Environ Sci. 2020;13:4609. https://doi.org/10.1039/D0EE02833A.

[4] Yang HZ, Shang L, Zhang QH, Shi R, Waterhouse GIN, Gu L, Zhang TR. A universal ligand mediated method for large scale synthesis of transition metal single atom catalysts. Nat Commun. 2019;10:4585. https://doi.org/10.1038/s41467-019-12510-0.

[5] Li JJ, Zhang ZC. K^+-enhanced electrocatalytic CO_2 reduction to multicarbon products in strong acid. Rare Met. 2022;41(3):723. https://doi.org/10.1007/s12598-021-01862-6.

[6] Jia YF, Li F, Fan K, Sun LC. Cu-based bimetallic electrocatalysts for CO_2 reduction. Adv Powder Mater. 2022;1(1):100012. https://doi.org/10.1016/j.apmate.2021.10.003.

[7] Wang YC, Huang ZS, Lei YP, Wu J, Bai Y, Zhao X, Liu MJ, Zhan LS, Tang SH, Zhang XB, Luo FH, Xiong X. Bismuth with abundant defects for electrocatalytic CO_2 reduction and Zn-CO_2 batteries. Chem Commun. 2022;58:3621. https://doi.org/10.1039/D2CC00114D.

[8] Wu ZX, Wu HB, Cai WQ, Wen ZH, Jia BH, Wang L, Jin W, Ma TY. Engineering bismuth-tin interface in bimetallic aerogel with a 3D porous structure for highly selective electrocatalytic CO_2 reduction to HCOOH. Angew Chem Int Ed. 2021;60(22):12554. https://doi.org/10.1002/anie.202102832.

[9] Jing HY, Zhu P, Zheng XB, Zhang ZD, Wang DS, Li YD. Theory-oriented screening and discovery of advanced energy transformation materials in electrocatalysis. Adv Powder Mater. 2022;1(1):100013. https://doi.org/10.1016/j.apmate.2021.10.004.

[10] Liu M, Wang YR, Ding HM, Lu M, Gao GK, Dong LZ, Li Q, Chen YF, Li SL, Lan YQ. Self-assembly of anthraquinone covalent organic frameworks as 1D superstructures for highly efficient CO_2 electroreduction to CH_4. Sci Bull. 2021;66(16):1659. https://doi.org/10.1016/j.scib.2021.05.001.

[11] Wang YC, Wang QC, Wu J, Zhao X, Xiong Y, Luo FH, Lei YP. Asymmetric atomic sites make different: recent progress in electrocatalytic CO_2 reduction. Nano Energy. 2022;103:107815. https://doi.org/10.1016/j.nanoen.2022.107815.

[12] Yin CY, Li Q, Zheng J, Ni YQ, Wu HQ, Kjøniksen AL, Liu CT, Lei YP, Zhang Y. Progress in regulating electronic structure strategies on Cu-based bimetallic catalysts for CO_2 reduction reaction. Adv Powder Mater. 2022;1(4):100055. https://doi.org/10.1016/j.apmate.2022.100055.

[13] Liu ST, Wang C, Wu JH, Tian BL, Sun YM, Lv Y, Mu ZY, Sun YX, Li XS, Wang FY, Wang YQ, Tang LY, Wang P, Li YF, Ding MN. Efficient CO_2 electroreduction with a monolayer Bi_2WO_6 through a metallic intermediate surface state. ACS Catal. 2021;11(20):12476. https://doi.org/10.1021/acscatal.1c02495.

[14] Liu BW, Xie Y, Wang XL, Gao C, Chen ZM, Wu J, Meng HY, Song ZC, Du SC, Ren ZY. Copper-triggered delocalization of bismuth p-orbital favours high-throughput CO_2 electroreduction. Appl Catal B Environ. 2022;301:120781. https://doi.org/10.1016/j.apcatb.2021.120781.

[15] Chen D, Wang YL, Liu DY, Liu H, Qian C, He HY, Yang J. Surface composition dominates the electrocatalytic reduction of CO_2 on ultrafine CuPd nanoalloys. Carbon Energy. 2020;2(3):443. https://doi.org/10.1002/cey2.38.

[16] Yuan YL, Wang QY, Qiao Y, Chen XL, Yang ZL, Lai WC, Chen TW, Zhang GH, Duan HG, Liu M, Huang HW. In situ structural reconstruction to generate the active sites for CO_2 electroreduction on bismuth ultrathin nanosheets. Adv Energy Mater. 2022;12(29):2200970. https://doi.org/10.1002/aenm.202200970.

[17] Li YZ, Chen JL, Chen S, Liao XL, Zhao TT, Cheng FY, Wang H. In situ confined growth of bismuth nanoribbons with active and robust edge sites for boosted CO_2 electroreduction. ACS Energy Lett. 2022;7(4):1454. https://doi.org/10.1021/acsenergylett.2c00326.

[18] Liu SQ, Shahini E, Gao MR, Gong L, Sui PF, Tang T, Zeng HB, Luo JL. Bi_2O_3 nanosheets grown on carbon nanofiber with inherent hydrophobicity for high-performance CO_2 electroreduction in a wide potential window. ACS Nano. 2021;15(11):17757. https://doi.org/10.1021/acsnano.1c05737.

[19] Wang YC, Xu L, Zhan LS, Yang PY, Tang SH, Liu MJ, Zhao X, Xiong Y, Chen ZY, Lei YP. Electron accumulation enables Bi efficient CO_2 reduction for formate production to boost clean Zn-CO_2 batteries. Nano Energy. 2022;92:106780. https://doi.org/10.1016/j.nanoen.2021.106780.

[20] Deng PL, Wang HM, Qi RJ, Zhu JX, Chen SH, Yang F, Zhou L, Qi K, Liu HF, Xia BY. Bismuth oxides with enhanced bismuth-oxygen structure for efficient electrochemical reduction of carbon dioxide to formate. ACS Catal. 2020;10(1):743. https://doi.org/10.1021/acscatal.9b04043.

[21] Wei CH, Sg G, Ma W, Mei SX, Xiang B, Gao B. Recent progress of bismuth-based electrode materials for advanced sodium ion batteries anode. Chin J Rare Met. 2021;45(5):611. https://doi.org/10.13373/j.cnki.cjrm.XY20070021.

[22] Sui PF, Xu CY, Zhu MN, Liu SB, Liu QX, Luo JL. Interface-induced electrocatalytic enhancement of CO_2-to-formate conversion on heterostructured bismuth-based catalysts. Small. 2022;18(1):2105682. https://doi.org/10.1002/smll.202105682.

[23] Wang JJ, Li XP, Cui BF, Zhang Z, Hu XF, Ding J, Deng YD, Han XP, Hu WB. A review of non-noble metal-based electrocatalysts for CO_2 electroreduction. Rare Met. 2021;40(11):3019. https://doi.org/10.1007/s12598-021-01736-x.

[24] Li Q, Wang YC, Zeng J, Zhao X, Chen C, Wu QM, Chen LM, Chen ZY, Lei YP. Bimetallic chalcogenides for electrocatalytic

CO_2 reduction. Rare Met. 2021;40(12):3442. https://doi.org/10.1007/s12598-021-01772-7.
[25] Zhang Y, Li FW, Zhang XL, Williams T, Easton CD, Bond AM, Zhang J. Electrochemical reduction of CO_2 on defect-rich Bi derived from Bi_2S_3 with enhanced formate selectivity. J Mater Chem A. 2018;6:4714. https://doi.org/10.1039/C8TA00023A.
[26] Xu WW, Lu ZY, Sun XM, Jiang L, Duan X. Superwetting electrodes for gas-involving electrocatalysis. Acc Chem Res. 2018;51(7):1590. https://doi.org/10.1021/acs.accounts.8b00070.
[27] Zhong Y, Xu Y, Ma J, Wang C, Sheng SY, Cheng CT, Li MX, Han L, Zhou LL, Cai Z, Kuang Y, Liang Z, Sun XM. An artificial electrode/electrolyte interface for CO_2 electroreduction by cation surfactant self-assembly. Angew Chem Int Ed. 2020;59(43):19095. https://doi.org/10.1002/anie.202005522.
[28] Sheng XD, Ge WX, Jiang HL, Li CZ. Engineering Ni-N-C catalyst microenvironment enabling CO_2 electroreduction with nearly 100% CO selectivity in acid. Adv Mater. 2022. https://doi.org/10.1002/adma.202201295.
[29] Shi R, Guo JH, Zhang XR, Waterhouse GIN, Han ZJ, Zhao YX, Shang L, Zhou C, Jiang L, Zhang TR. Efficient wettability-controlled electroreduction of CO_2 to CO at Au/C interfaces. Nat Commun. 2021;11:3028. https://doi.org/10.1038/s41467-020-16847-9.
[30] Cai Z, Zhang YS, Zhao YX, Wu YS, Xu WW, Wen XM, Zhong Y, Zhang Y, Liu W, Wang HL, Kuang Y, Sun XM. Selectivity regulation of CO_2 electroreduction through contact interface engineering on superwetting Cu nanoarray electrodes. Nano Res. 2019;12:345. https://doi.org/10.1007/s12274-018-2221-7.
[31] Lebedev YA, Korolev YM, Polikarpov VM, Ignat'eva LN, Antipov EM. X-ray powder diffraction study of polytetrafluoroethylene. Crystallogr Rep. 2010;55:609. https://doi.org/10.1134/S1063774510040127.
[32] Ding P, Zhang J, Han N, Zhou Y, Jia L, Li YG. Simultaneous power generation and CO_2 valorization by aqueous Al-CO_2 batteries using nanostructured Bi_2S_3 as the cathode electrocatalyst. J Mater Chem A. 2020;8:12385. https://doi.org/10.1039/D0TA03761C.
[33] Yang XX, Deng PL, Liu DY, Zhao S, Li D, Wu H, Ma YM, Xia BY, Li MT, Xiao CH, Ding SJ. Partial sulfuration-induced defect and interface tailoring on bismuth oxide for promoting electrocatalytic CO_2 reduction. J Mater Chem A. 2020;8:2472. https://doi.org/10.1039/C9TA11363K.
[34] Wang YT, Li YH, Liu JZ, Dong CX, Xiao CQ, Cheng L, Jiang HL, Jiang H, Li CZ. $BiPO_4$-derived 2D nanosheets for efficient electrocatalytic reduction of CO_2 to liquid fuel. Angew Chem Int Ed. 2021;60(14):7681. https://doi.org/10.1002/anie.202014341.
[35] Li JF, Li ZY, Liu XM, Li CY, Zheng YF, Yeung KWK, Cui ZD, Liang YQ, Zhu SL, Hu WB, Qi YJ, Zhang TJ, Wang XB, Wu SL. Interfacial engineering of Bi_2S_3/$Ti_3C_2T_x$ MXene based on work function for rapid photo-excited bacteria-killing. Nat Commun. 2021;12:1224. https://doi.org/10.1038/s41467-021-21435-6.
[36] Wang Y, Liu M, Hao SQ, Li Y, Li QQ, Liu FY, Lai YQ, Li J, Wolverton C, Dravid VP, Jiang LX. Synergistic defect- and interfacial-engineering of a Bi_2S_3-based nanoplate network for high-performance photoelectrochemical solar water splitting. J Mater Chem A. 2022;10:7830. https://doi.org/10.1039/D1TA09961B.
[37] Rabin O, Perez JM, Grimm J, Wojtkiewicz G, Weissleder R. An X-ray computed tomography imaging agent based on long-circulating bismuth sulphide nanoparticles. Nat Mater. 2006;5:118. https://doi.org/10.1038/nmat1571.
[38] Wu SW, Li YZ, Zhang Q, Hu QQ, Wu JC, Zhou CY, Zhao XJ. Formation of NiCo alloy nanoparticles on Co doped Al_2O_3 leads to high fuel production rate, large light-to-fuel efficiency, and excellent durability for photothermocatalytic CO_2 Reduction. Adv Energy Mater. 2020;10(42):2002602. https://doi.org/10.1002/aenm.202002602.
[39] Zeng ZP, Gan LY, Yang HB, Su XZ, Gao JJ, Liu W, Matsumoto H, Gong J, Zhang JM, Cai WZ, Zhang ZY, Yan YB, Liu B, Chen P. Orbital coupling of hetero-diatomic nickel-iron site for bifunctional electrocatalysis of CO_2 reduction and oxygen evolution. Nat Commun. 2022;12:4088. https://doi.org/10.1038/s41467-021-24052-5.
[40] Phu TT, Daiyan R, Fusco Z, Ma ZP, Amal R, Tricoli A. Nanostructured β-Bi_2O_3 fractals on carbon fibers for highly selective CO_2 electroreduction to formate. Adv Funct Mater. 2020;30(3):1906478. https://doi.org/10.1002/adfm.201906478.
[41] Wu D, Wang XW, Fu XZ, Luo JL. Ultrasmall Bi nanoparticles confined in carbon nanosheets as highly active and durable catalysts for CO_2 electroreduction. Appl Catal B Environ. 2021;284:119723. https://doi.org/10.1016/j.apcatb.2020.119723.
[42] Pang RC, Tian PF, Jiang HL, Zhu MH, Su XZ, Wang Y, Yang XL, Zhu YH, Song L, Li CZ. Tracking structural evolution: operando regenerative CeO_x/Bi interface structure for high-performance CO_2 electroreduction. Natl Sci Rev. 2021;8(7):nwaa187. https://doi.org/10.1093/nsr/nwaa187.
[43] Wang WB, Wang ZT, Yang RO, Duan JY, Liu YW, Nie AM, Li HQ, Xia BY, Zhai TY. In situ phase separation into coupled interfaces for promoting CO_2 electroreduction to formate over a wide potential window. Angew Chem Int Ed. 2021;60(42):22940. https://doi.org/10.1002/anie.202110000.
[44] Li Q, Wang YC, Zeng J, Wu QM, Wang QC, Sun L, Xu L, Ye T, Zhao X, Chen L, Chen ZY, Chen LM, Lei YP. Phosphating-induced charge transfer on CoO/CoP interface for alkaline H_2 evolution. Chin Chem Lett. 2021;32(11):3355. https://doi.org/10.1016/j.cclet.2021.03.063.
[45] Xing Z, Hu X, Feng XF. Tuning the microenvironment in gas-diffusion electrodes enables high-rate CO_2 electrolysis to formate. ACS Energy Lett. 2021;6(5):1694. https://doi.org/10.1021/acsenergylett.1c00612.
[46] Lin J, Yan SL, Zhang CX, Hu Q, Cheng ZM. Hydrophobic electrode design for CO_2 electroreduction in a microchannel reactor. ACS Appl Mater Interfaces. 2022;14(6):8623. https://doi.org/10.1021/acsami.1c23744.
[47] Wang ZY, Wang C, Hu YD, Yang S, Yang J, Chen WX, Zhou H, Zhou FY, Wang LX, Du JY, Li YF, Wu YE. Simultaneous diffusion of cation and anion to access N, S co-coordinated Bi-sites for enhanced CO_2 electroreduction. Nano Res. 2021;14:2790. https://doi.org/10.1007/s12274-021-3287-1.
[48] Zhang XY, Li WJ, Wu XF, Liu YW, Chen JC, Zhu MH, Yuan HY, Dai S, Wang HF, Jiang Z, Liu PF, Yang HG. Selective methane electrosynthesis enabled by a hydrophobic carbon coated copper core-shell architecture. Energy Environ Sci. 2022;15:234. https://doi.org/10.1039/D1EE01493E.
[49] Mizuno T, Naitoh A, Ohta K. Electrochemical reduction of CO_2 in methanol at −30 °C. J Electroanal Chem. 1995;391(1–2):199. https://doi.org/10.1016/0022-0728(95)03936-B.
[50] Chi LP, Niu ZZ, Zhang XL, Yang PP, Liao J, Gao FY, Wu ZZ, Tang KB, Gao MR. Stabilizing indium sulfide for CO_2 electroreduction to formate at high rate by zinc incorporation. Nat Commun. 2021;12:5835. https://doi.org/10.1038/s41467-021-26124-y.
[51] Xu QC, Zhang JH, Zhang HX, Zhang LY, Chen L, Hu YJ, Jiang H, Li CZ. Atomic heterointerface engineering overcomes the activity limitation of electrocatalysts and promises highly-efficient alkaline water splitting. Energy Environ Sci. 2021;14:5228. https://doi.org/10.1039/D1EE02105B.